Predicting Cortical Bone Resorption in Disuse Condition Caused by Transient Muscle Paralysis

[1]Himanshu Shekhar, [1]Sanjay Singh, [1]Jitendra Prasad*

[1]Indian Institute of Technology Ropar, Rupnagar, Punjab, 140001

Himanshu Shekhar

Department of Mechanical Engineering,

Indian Institute of Technology Ropar,

Rupnagar, Punjab, India, 140001

Email- himanshu.19mez0001@iitrpr.ac.com

Sanjay Singh

Department of Mechanical Engineering,

Indian Institute of Technology Ropar,

Rupnagar, Punjab, India, 140001

email- 2017mez0012@iitrpr.ac.in

Jitendra Prasad*

Department of Mechanical Engineering,

Indian Institute of Technology Ropar,

Rupnagar, Punjab, India, 140001

email- jprasad@iitrpr.ac.in

*Corresponding author

Abstract

Load removal from the load-bearing bone, such as in the case of extended space travel and prolonged bed rest, harms bone health and leads to severe bone loss. However, the constitutive idea relating the quantity of bone loss to the absence of physiological loading is poorly understood. This work attempts to develop a mathematical model that predicts cortical bone loss at three sections: 'distal,' 'mid-section,' and 'proximal' along the length of a mouse tibia. Load-induced interstitial fluid flow-based dissipation energy density has been adopted as a stimulus to trigger mechanotransduction. The developed model takes the loss of stimulus due to the disuse of bone as an input and predicts the quantity of bone loss with spatial accuracy.

In the loaded bone, the fluid velocity is found to be maximum at the endocortical surface and negligible at the periosteal surface due to the permeable and impermeable boundary conditions, respectively, at the two surfaces. In case of disuse of bone, there is no fluid flow, which leads to a more significant loss of fluid flow at the endocortical surface. This loss of fluid flow coincides with the botulinum toxin (Botox)-induced endocortical bone loss data in the literature. Motivated by this fact, we hypothesized that the bone loss site would be the site of maximum stimulus loss due to disuse.

To test the hypothesis, we calculated stimulus loss, i.e., loss of dissipation energy density due to bone disuse, based on the poroelastic analysis of the bone using a finite element method. A novel mathematical model has been then developed that successfully relates this loss of stimulus to the in-vivo bone loss data in the literature. According to the developed model, the site-specific mineral rate is found to be proportional to the square root of the loss of dissipation energy density. To the author's best knowledge, this model is the first of its kind to compute site-specific bone loss. The developed model can be extended to predict bone loss due to other disuse conditions such as long space travel, prolonged bed rest, etc.

Keywords: Cortical bone loss, disuse of bone, fluid flow, poroelasticity, mathematical modeling, dissipation energy density, botulinum toxin (Botox), unloading

List of Symbols

σ_{ij}	Stress tensor
ε_{ij}	Strain tensor
μ	Viscosity of fluid
p	Pore pressure
ν	Poisson's ratio
$\boldsymbol{v}^{fl}$	Fluid velocity
DED	Dissipation energy density
ϕ	Total dissipation energy density
n_p	Porosity
MRR_{exp}^{i}	Experimental mineral resorption rate at ith point of interest
MRR_{model}^{i}	Model mineral resorption rate at the ith point of interest
q	Fluid flow rate
δ_{ij}	Kronecker delta
Δ	Volumetric strain

1. Introduction

The bone is an example of an optimized structure. The internal architecture of a bone is adapted to the external mechanical load exerted during daily physical activity (Warden et al., 2014) (Huddleston et al., 1980) (Haapasalo et al., 2000) (Charalambous, 2014). However, in some cases, these physical activities are disturbed; for example, long space travel (Lang et al., 2004) (Vico et al., 2000), prolonged bed rest (Hargens and Vico, 2016) (Rittweger et al., 2009), and paralysis of the lower extremity due to the spinal cord injury(Lee et al., 1997). The deficit in mechanical load on the load-bearing bone due to the reason above is undesirable and leads to severe bone loss (Brent et al., 2021). A recent study reveals that the microgravity environment in spaceflight is so harmful that even one year after the mission, the lost bone tissue is not entirely recovered, which may lead to osteoporosis (Gabel et al., 2022). Similarly, the studies involving the Russian Mir and the International Space Station reported that crew members of extended space flights suffer from around 1.2-1.5% bone mass per month from their proximal femur. Likewise, six months of the mission caused a loss of cortical density by 2% from the tibial diaphysis. However, this space-flight-based study is found to be very expensive. Therefore, bedridden, hindlimb unloading, and botulinum toxin (Botox)-induced bone loss have been made to simulate such a study (Rolvien and Amling, 2021). For example, 90 days

of bed rest causes 1-2% of the mean cortical loss from the tibial site (Rittweger et al., 2005). Botox-induced endo-cortical bone loss was heterogeneous along the tibial length (Ausk et al., 2012). However, the cellular and molecular mechanism behind how the loss in the mechanical environment is related to bone tissue deterioration needs to be better understood. It has been well recognized that the bone cell osteocyte acts as a mechano-sensor (Qin et al., 2020) (Klein-Nulend et al., 2013) and is densely connected through the lacune canaliculi network (LCN) in the bone matrix. Experimental studies provide insight into the fact that the load-induced fluid flow inside the LCN helps in the mass transport necessary to enhance the metabolic function of the bone cells, i.e., osteocytes, which are crucial for maintaining bone health. Moreover, the load-induced fluid flow has gained attention as a prime stimulus for bone's mechanotransduction(Gururaja et al., 2005) (Fritton and Weinbaum, 2009) (Verbruggen et al., 2014) (Tiwari and Prasad, 2017). Another study illustrates that the load-induced fluid flow through LCN exerts shear stresses on the cell wall (Weinbaum et al., 1994), which activates the mechano-sensing cell osteocytes. In addition, the tracer technique also confirms the existence of the fluid flow inside the LCN (Knothe Tate and Knothe 2000) experimentally. However, in-vivo studies have been unable to measure exact fluid velocity due to the inaccessibility of the LCN. Hence, the finite element method have been used to quantify the fluid velocity (Meslier and Shefelbine, 2023) (Steck et al., 2003) (Pereira et al., 2015)(Smit, 2022) (Kumar et al., 2011) (Van Tol et al., 2020) (Teresa et al., 2020). Recently, one study confirmed that Botox-induced muscle paralysis significantly affects the bone's morphology (Gatti et al., 2019), leading to decreased fluid velocity around the osteocyte (Gatti et al., 2021), which motivates us to consider the loss of fluid flow for modelling bone loss.

When bone is mechanically strained during the physiological loading, a pressure gradient is generated inside the LCN, forcing fluid to flow in the canalicular channels (Fig 1). Due to the viscous nature of the fluid, it exerts shear stress on the cell membrane, and energy is dissipated. The dissipated energy, which is a function of fluid velocity, is assumed to be a stimulus to the mechano-sensing cell, i.e., osteocyte (Kumar et al., 2011). It is evident from the literature that in the case of a loaded bone, the resultant fluid velocity is higher at the endocortical surface while negligible at the periosteal surface (Singh et al., 2023) due to the permeable and impermeable nature of the respective surfaces (Fan et al., 2016). Botox-induced calf muscle paralysis pauses the locomotion, resulting in zero strain on bone and, thus, no fluid flow inside the LCN Fig 1(d). Therefore, there is likely to be a more significant loss of fluid velocity at the

endocortical surface, which coincides with the in-vivo Botox-induced bone loss pattern at the endocortical surface.

The present work considers the loss of mechanical stimulus, i.e., loss of fluid flow-based dissipation energy density due to the disuse of bone. It develops a mathematical model that can correctly predict cortical bone loss. The developed model was validated using the available Botox-induced bone loss data in the literature (Ausk et al., 2012). Statistical tests were performed to quantify how accurately the model predicted the in-vivo results. The developed model can be extended on the availability of relevant experimental data to predict remaining disuse conditions such as long space travels, prolonged bed rest, etc. The rest of the paper has been organized as follows. Section 2 describes the adopted methodology. Section 3 presents the results, which have been discussed in section 4. Conclusions have been drawn in section 5.

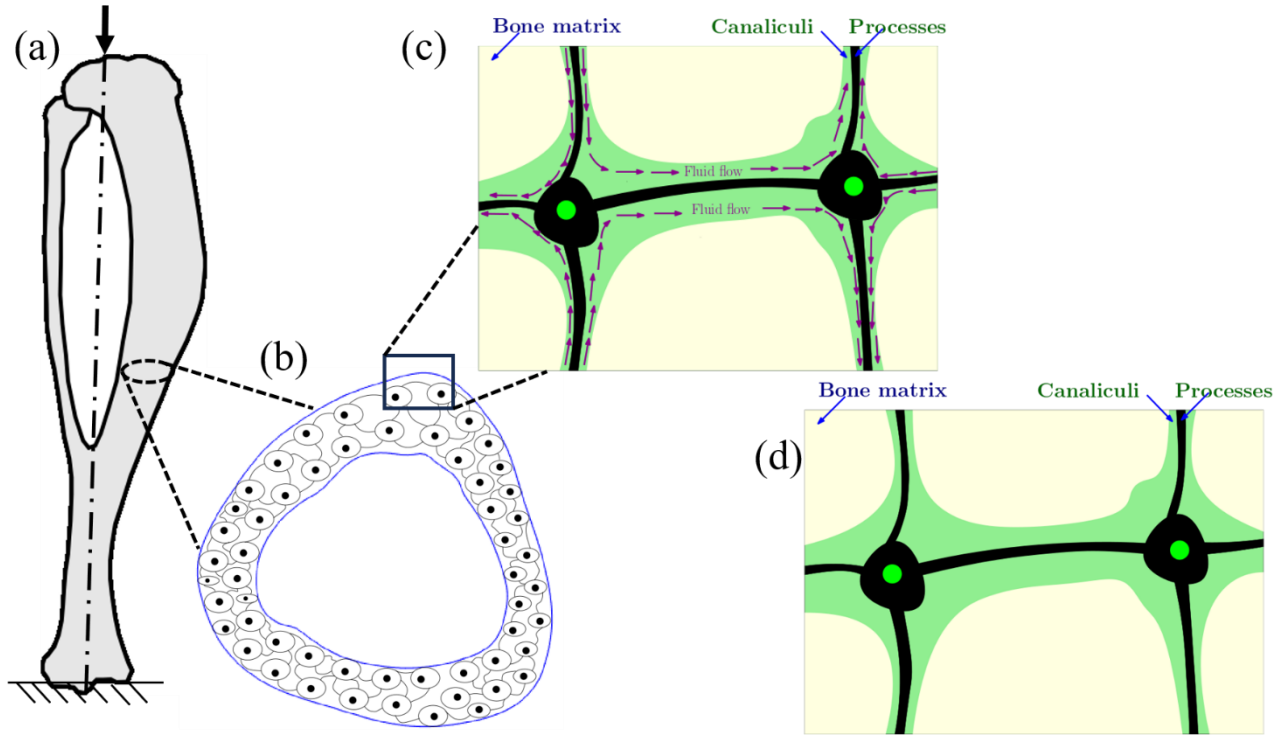

Figure 1: Comparison of fluid flow inside the LCN, physiologically loaded vs disused tibia: (a) axially loaded tibia, (b) schematic of the osteocytes' network at a cross-section of interest, (c) fluid flow inside an LCN (arrows indicate fluid flow) of a physiologically loaded tibia, (d) no fluid flow inside the LCN in case of disuse of the bone.

2. Methods

2.1 Theory of Poroelasticity

Mouse tibia was considered a linear isotropic porous material consisting of a solid matrix and fluid-saturated pores (Cowin, 1999). The constitutive equations for such material are as follows (Biot, 1941).

$$\sigma_{ij} = 2G\varepsilon_{ij} + \frac{2G\nu}{1-2\nu}\varepsilon_{kk}\,\delta_{ij} - \alpha p\delta_{ij} \tag{1}$$

$$\zeta = \alpha\Delta + \frac{p}{Q} \tag{2}$$

where σ_{ij} and ϵ_{ij} are stress and strain tensors, respectively (i or j represents the Cartesian coordinates, i.e., i or j=1,2,3 corresponds to the x, y, z coordinates). G and ν are the modulus of rigidity and Poisson's ratio, respectively. p is the interstitial pore pressure, ζ is the increment of the water volume per unit volume of the solid matrix, δ_{ij} is the Kronecker delta (i.e., $\delta_{ij} = 1$ if i=j; $\delta_{ij} = 0$ otherwise), Δ is the dilation that represents the volumetric strain developed in the pore, α, and $\frac{1}{Q}$ are the constants.

Equation (3) describes the fluid flow rate through a porous media following Darcy's law:

$$q_i = -\frac{k}{\mu}\frac{\partial p}{\partial x_i} \tag{3}$$

where, q_i is the fluid mass flow rate, while k and μ represent the isotropic intrinsic permeability and dynamic viscosity of the fluid, respectively.

The mass balance equation is as follows:

$$\frac{\partial\zeta}{\partial t} = -\frac{\partial q_1}{\partial x_1} - \frac{\partial q_2}{\partial x_2} - \frac{\partial q_3}{\partial x_3} \tag{4}$$

The above equations finally lead to the following differential equation that needs to be solved:

$$k\nabla^2 p = \alpha\frac{\partial\Delta}{\partial t} + \frac{1}{Q}\frac{\partial p}{\partial t} \tag{5}$$

Additionally, the linear momentum balance can be written as

$$G\nabla^2 u_i + \frac{G}{1-2\nu}\frac{\partial\Delta}{\partial x_i} = \alpha\frac{\partial p}{\partial x_i} \tag{6}$$

Where u_i is the displacement of the solid matrix. The above Eqs. (5) and (6) together have 4 unknowns to be solved for – 3 displacements components (viz. u_1, u_2 and u_3) and the fluid pore pressure p. The problem was solved using a finite element commercial ABAQUS software(Abaqus, 2014), as detailed in section 2.6.

2.2 Cage Activity of a Mouse

The mice were monitored in a cage for 24 hrs, and their activities were captured (Hasriadi et al., 2021)—typical cage activities involved locomotion, rearing, immobilization, and climbing.

- **Locomotion**: The most prominent activity of a mouse in a cage was found to be locomotion. During the locomotion, the tibia is subjected to ground reaction forces, which can be resolved into axial compression and transverse shear forces (Prasad et al., 2010). It was found that the magnitude of shear force is very minimal compared to the axial component and hence can be ignored (Mertiya et al., 2022) (Gatti et al., 2021). This leads to only axial force on the mouse tibia. It is seen that axial compression on the tibia is prominent during the locomotion of a mouse.
- **Rearing**: Rearing was the second most cage activity of a mouse. During rearing, a mouse first stands on its Hindlimb, which leads to pure axial loading on the murine tibia.
- **Immobilization**: Immobilization of a mouse exerts static loading on the mouse tibia. Moreover, it has already been established that static loading does not lead to new bone formation (Derbyshire, 1985).
- **Climbing**: Climbing leads to no ground reaction forces on the mouse tibia.

The above observation of a caged mouse suggests that the axial loading is typically significant on the tibia of a caged mouse.

2.3 Porosity and permeability of cortical bone

The cortical bone has porosities of different length scales (Cowin, 1999), such as vascular porosity and lacune-canalicular porosity, which influence bone permeability. It is widely accepted in the literature that the loading-induced fluid flow inside the LCN plays an important role in bone mechanotransduction. Accordingly, only LCN porosity has been considered, viz. $3.79 \times 10^{-21}\ m^2$(Zhou et al., 2008), as also presented in Table 1.

2.4 Loading and boundary conditions

The physiological loading in the case of a caged mouse is dominated by axial loading (Fig 2(a)). To mimic the physiological condition, a Haversine loading waveform having a frequency of 1 Hz (Fig 2(c)) was considered in accordance with the literature (Gatti et al., 2021). The

axial component (1.3 N) of ground reaction force exerted during a physiological loading conditions was obtained from the literature (Prasad et al., 2010). In accordance with the literature, the periosteal and endocortical bone surfaces were assumed to be completely impermeable and permeable, respectively (Singh et al., 2023) (Gatti et al., 2021) (Fan et al., 2016) implemented through zero-flow and zero-pressure boundary conditions respectively (Fig. 2(b)).

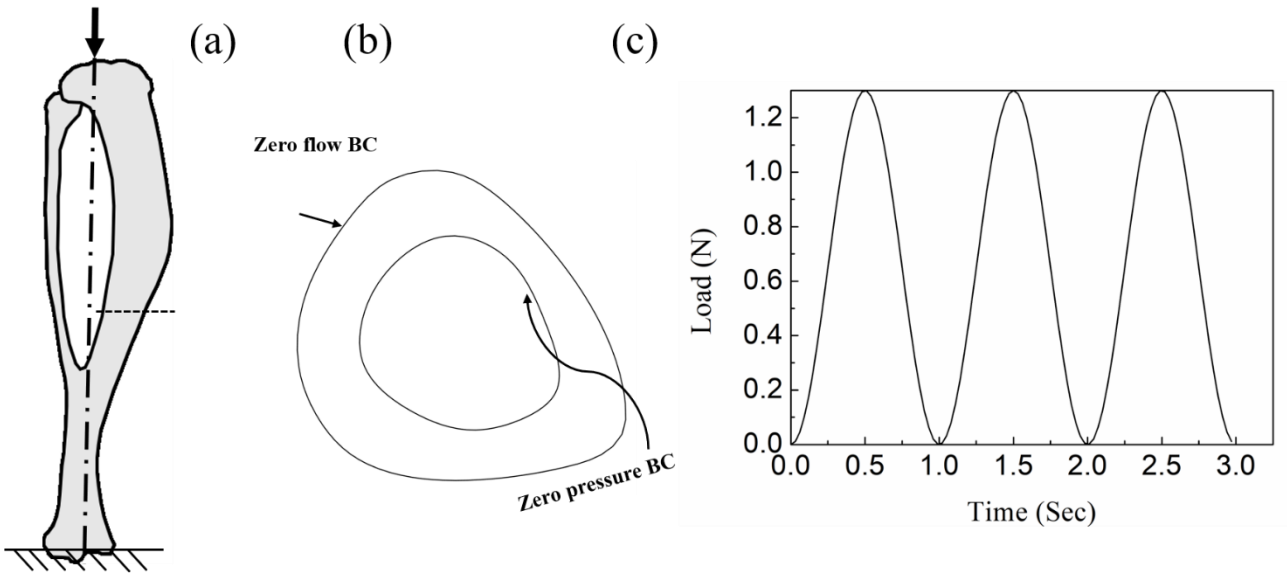

Figure 2: Loading and boundary conditions (a) cage activity is idealized as an axial loading (b) periosteal and endocortical surface of the bone was prescribed zero-fluid-flow and zero-pressure ($p = 0$) conditions, respectively. (c) To mimic the physiological loading, a Haversine loading waveform of 1 Hz frequency was assumed.

2.5 Bone geometry

The whole 3D model of a mouse tibia is computationally expensive, and hence, the tibia was idealized as a prismatic bar having a cross-section similar to that of a C57BL6J, 16-week, young-adult mouse given in the literature. Three prismatic bars (each with a length of 10 mm) with cross-sections identical to the distal, mid-shaft, and proximal cross-sections studied by Ausk et al. (Ausk et al., 2012) were created. Three prismatic bars along the tibial length, are shown in Fig 3.

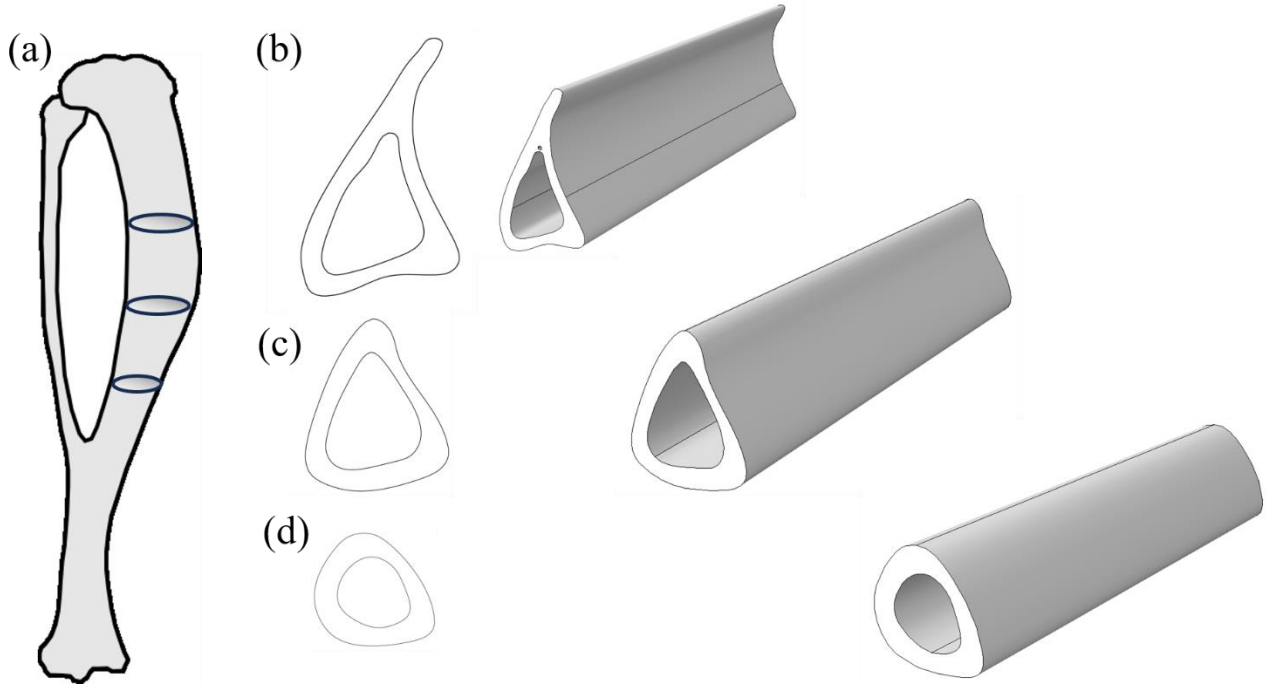

Figure 3: The bone (a) is idealized as a prismatic bar (b) of length 10 mm and having a cross-section similar to that of the "proximal section", (c) "mid-section" and (d) "distal section" studied by Ausk et al. (Ausk et al., 2012)

2.6 Finite Element Analysis

The finite element problem was solved using the commercial software ABAQUS (Dassault System). To simulate fully or partially saturated fluid flow through porous media, the soil element (C3D8RP, continuous three-dimensional eight nodded reduced integration pore pressure hexahedral element) type was used, which is available in ABAQUS (Abaqus, 2014). These elements had 4 degrees of freedom (3 for the displacement and 1 for pore pressure) per node. The bone material was assumed to be a linear isotropic poroelastic material whose parameters were directly taken from Kumar et al. (Kumar et al., 2011) and have been shown in Table 1. To capture the fluid velocity inside the LCN, a coupled pore fluid diffusion stress analysis was performed using the ABAQUS software. The fluid velocity was computed at the integration point during the applied loading. The physiological-loading-induced strain and corresponding fluid flow velocity at the three sections viz at distal, mid-section, and proximal sections along the tibial length have been shown in Fig 4. The obtained strain patterns were verified according to the existing literature (Patel et al., 2014).

Table 1: Poroelastic material properties used in the simulations adapted from (Kumar et al., 2011) except the permeability value (Zhou et al., 2008)

Properties	Magnitude	Unit
Young's modulus of bone	12	GPa
Fluid bulk modulus	2.3	GPa
Solid bulk modulus	17	GPa
Porosity	0.05	
Poisson's Ration	0.3	
Intrinsic permeability (k)	3.79×10^{-21}	m^2

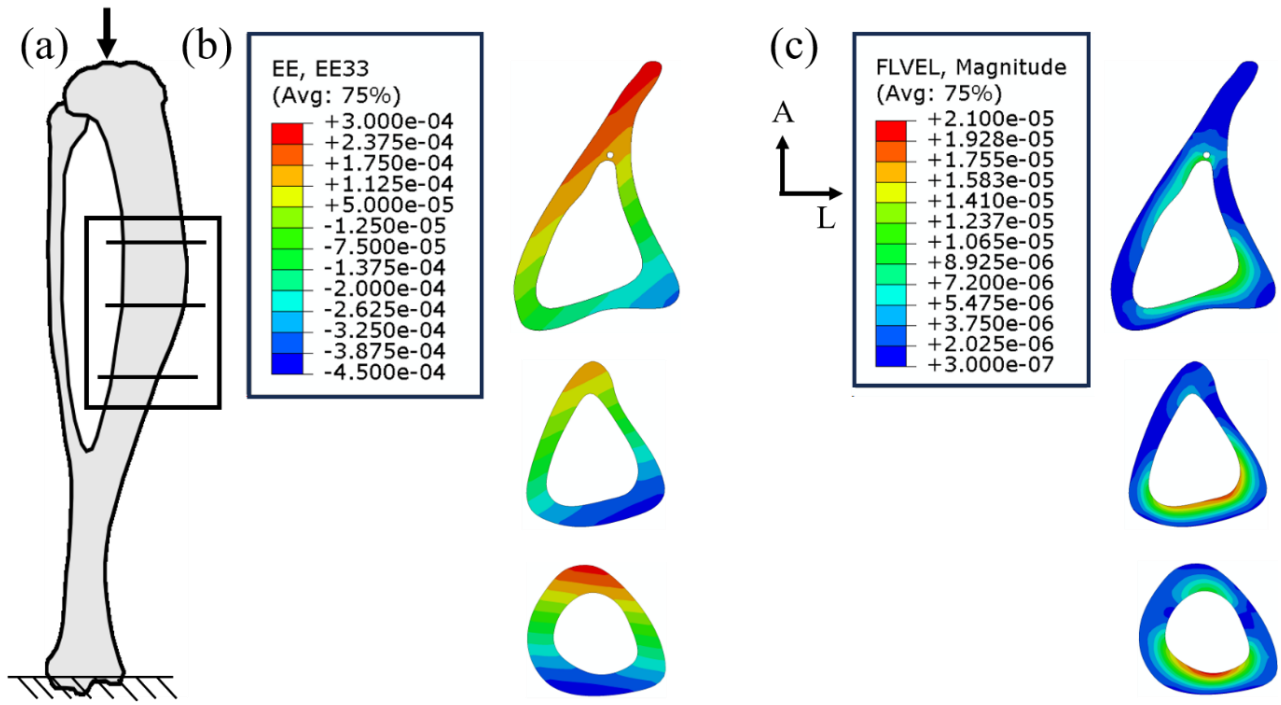

Figure 4: Axial loading environment of a mouse tibia (a) longitudinal strain (EE33) pattern along the tibial length, i.e., at distal, mid-section, and proximal section (b) corresponding fluid velocity (mm/s)

2.7 Botox-induced disuse Activity

Botox-induced calf muscle paralysis incapacitates the muscles to apply force on the tibia, which causes a loss of strain environment. We assume that the application of Botox leads to zero strain on the tibia and, hence, zero fluid velocity (Fig 5).

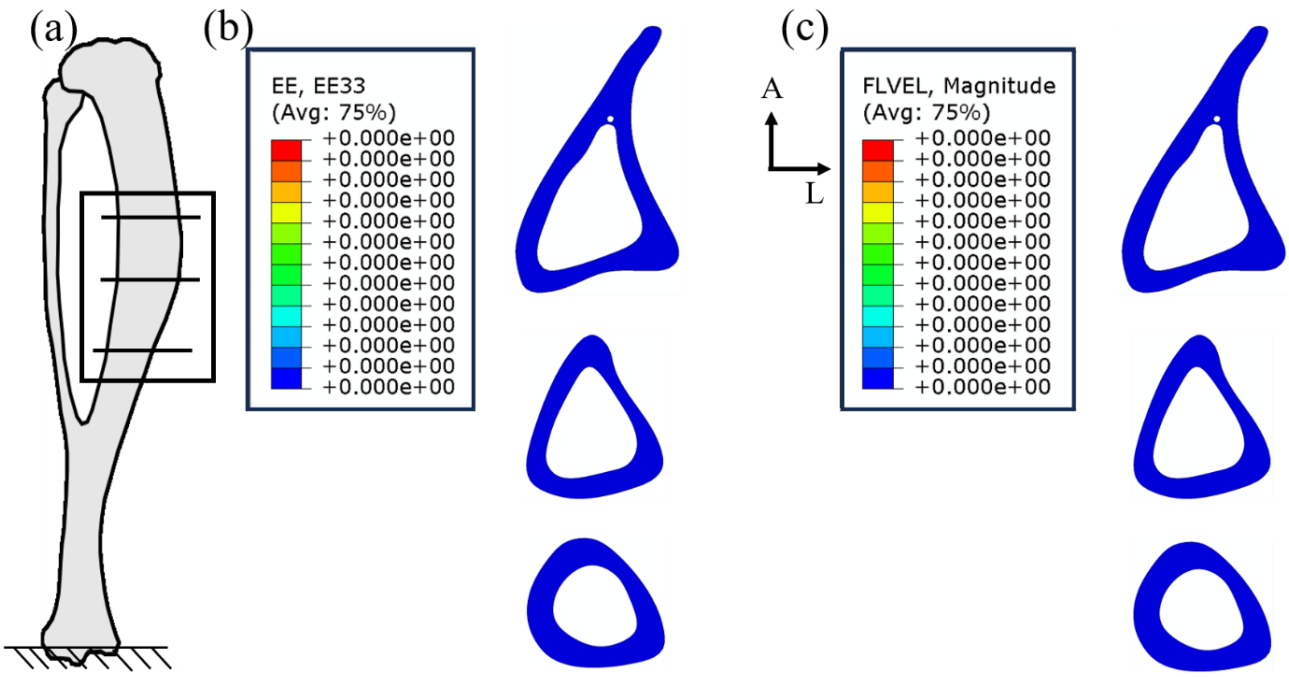

Figure 5: Botox-induced mechanical environment in a mouse tibia (a) a typical mouse tibia (b) strain pattern (zero strain everywhere) (c) fluid flow pattern (zero fluid flow throughout the cross-section)

2.8 Computation of fluid flow-based dissipation energy density

Load-induced viscous fluid flow inside LCN exerts shear stress on the osteocyte cell membrane, and energy is dissipated. The dissipated energy influences the mechano-sensing cell osteocyte, and further biochemical signalling pathways get activated. According to Kumar et al. (Kumar et al., 2011), the dissipation energy density (DED), which is a function of fluid velocity, can be calculated as:

$$DED = -n_p \boldsymbol{v}^{fl}.\nabla p = \frac{1}{2}\left(n_p \boldsymbol{v}^{fl}\right).\left(\frac{k}{\mu}\right)^{-1}.\left(n_p \boldsymbol{v}^{fl}\right) \tag{7}$$

Where $n_p$is the LCN porosity, $\boldsymbol{v}^{fl}$ is the fluid velocity. To capture the effect of the non-local behavior of osteocytes, a spherical zone of influence (ZOI) was considered (as shown in Fig 6), similar to the earlier study by Singh et al. (Singh et al., 2023). Considering the ZOI, the dissipation energy density was calculated using Eq. (8) at every ith node of interest. The total dissipation energy density $\phi = DED * N * d$. Where N is the no. of cycles and d is no. of days.

$$DED_i = \frac{\int_V \left(\int_0^T \frac{1}{2}\left(n_p \boldsymbol{v}^{fl}\right).\left(\frac{k}{\mu}\right)^{-1}.\left(n_p \boldsymbol{v}^{fl}\right)dt\right) f(|x|)dV}{\int_V f(|x|)dV} \tag{8}$$

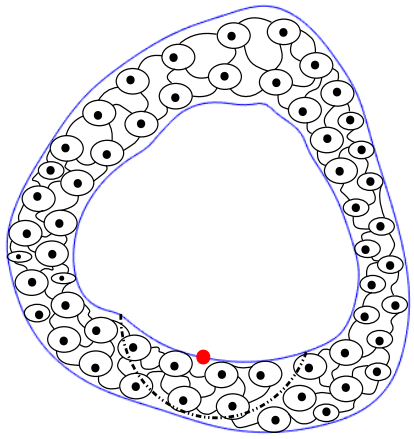

Figure 6: The non-local behavior of the osteocyte is captured through a spherical zone of influence. The red node shows the point of interest.

where $f(|x|) = e^{\left(-\frac{5|x|}{R}\right)}$ is a weighting function that weights the contribution of osteocytes that fall under the spherical zone of influence. The $|x|$ represents the distance between the node of interest and the position of osteocytes, while R represents the radius of the spherical zone.

2.9 Mineral Resorption Rate (MRR)

Exogenous loading-induced fluid flow inside the LCN has been widely accepted in the literature to correlate with bone adaptation. Recently, Sanjay et al. (Singh et al., 2023) have presented a robust formulation that shows that MAR (mineral apposition rate), i.e., rate of change of new bone thickness, is directly proportional to the square root of total dissipation energy density minus its threshold or reference value. That is,

$$MAR = A\left(\sqrt{\phi_c} - \sqrt{\phi_{phy}}\right), \tag{9}$$

where A is the remodelling rate, ϕ_c is the current dissipation energy density, while ϕ_{phy} represents the dissipation energy density to maintain bone homeostasis (under physiological loading conditions). In the disuse condition, the fluid velocity is zero, which leads $\sqrt{\phi_c}$ to a zero value. Hence, the expression of MAR is simplified to

$$MAR = -A\left(\sqrt{\phi_{phy}}\right) \tag{10}$$

Here, the negative sign shows bone loss, and hence, mineral resorption rate (MRR) can be written as

$$MRR_{model} = A\left(\sqrt{\phi_{phy}}\right) \tag{11}$$

Thus, MRR_{model} is directly proportional to the square root of the total dissipation energy density. The parameter A is a constant to be determined. The MRR ($\mu m^3/\mu m^2/day$) is defined as the total loss of bone volume per unit of bone surface area per unit time. For the sake of computational convenience, the endocortical bone surface was divided into 360 segments, and then MRR was calculated at every ith point (i.e., a common point of two consecutive segments) as

$$MRR^i_{model} = A\left(\sqrt{\phi_i}\right). \tag{12}$$

As an example, these points are shown in Fig. 7. The constant A was calculated by comparing the experimental bone loss data available in the literature. Experimental endocortical bone loss MRR^i_{exp} for each of the 360 points was computed from Fig 7 using an in-house MATLAB code. The optimization problem was formulated as a minimization of squared error:

$$Min\ f(A) = \sum_{i=1}^{i=360} \left(MRR^i_{exp} - MRR^i_{model}\right)^2 \tag{13}$$

The Levenberg Marquardt algorithm (Levenberg, 1944) available in MATLAB was used to fit the model in Eq. (12) to the experimental data, i.e. MRR^i_{exp} and find the optimal value of the constant A. The calculated optimal parameter A (6.82 $\frac{mm^2}{\sqrt{N}\ day}$) was then used to predict bone loss at the two remaining sections, viz., the mid and proximal sections. A statistical analysis (as detailed in section 2.10) was performed to compare the model prediction to the experimental values.

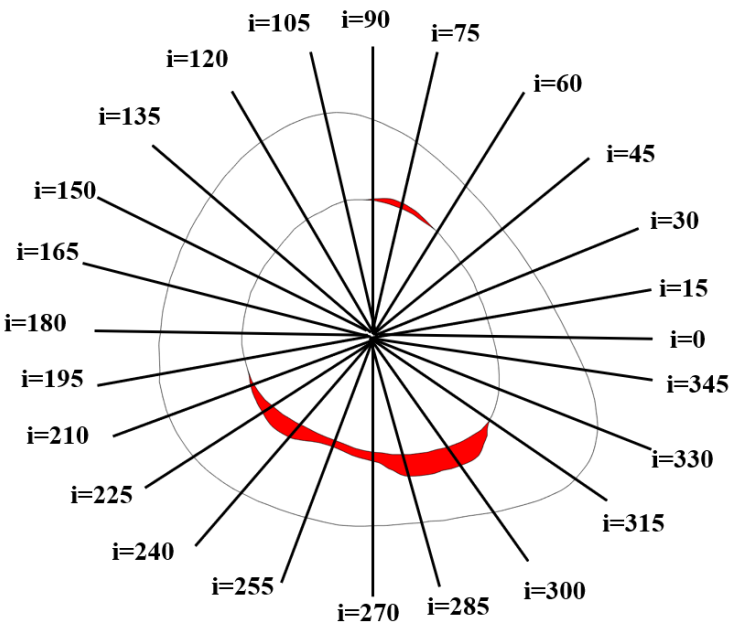

Figure 7: In-vivo cortical bone loss at the distal section of a tibia; endocortical bone surface was divided into 360 points (for clear visibility, the points have been drawn at every 15 degrees).

2.10 Statistical Analysis

A one-sample, two-tailed Student's t-test was used to compare the average bone resorption rate per unit bone surface (BRR/BS) values. A circular goodness-of-fit test, viz, Watson's U^2 test (WATSON, 1961), was used to compare the endocortical distribution of bone loss predicted by the model to the in-vivo results.

3. Results

3.1 Distal Section

The developed model was first used to predict cortical bone loss at the distal section. The BRR values have been compared in Fig. 8(a) through a histogram. The obtained site-specific bone loss distribution by the model was shown in Fig. 8(c), whereas the experimental bone loss was shown in Fig. 8(b). The statistical analysis showed that the model BRR/BS, 1.49 $\mu m^3/\mu m^2/day$, was not significantly different from the in-vivo BRR/BS, 1.15±0.67 $\mu m^3/\mu m^2/day$ ($p = 0.62$, Student's t-test). The predicted bone loss distribution was also found to be not significantly different from the in-vivo distribution ($p = 0.31$, Watson's U^2 test).

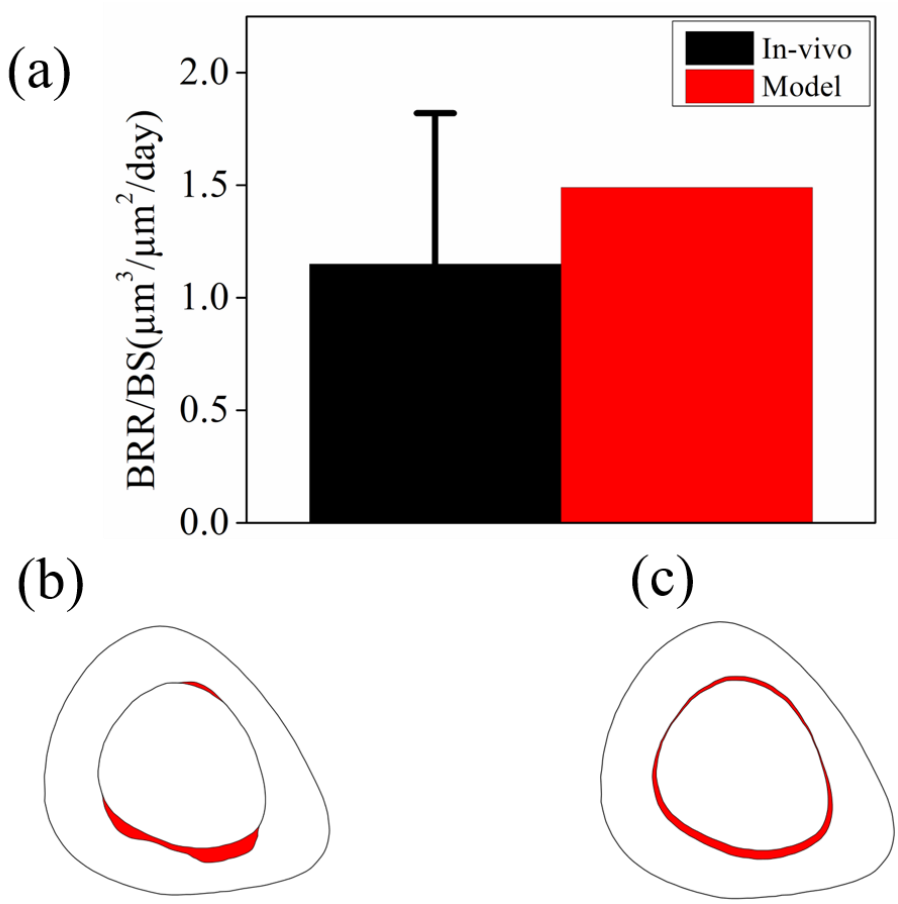

Figure 8: Comparison of model and experimental cortical bone loss at the distal section of a mouse tibia: (a) model BRR/BS is not significantly different from the in-vivo BRR/BS, (b) site-specific in-vivo bone loss (shown in red), (c) predicted bone loss by the model.

3.2 Mid-section

Mid-section cortical bone loss was also predicted using the same resorption rate A. The predicted and the in-vivo BRR/BS have been compared in Fig. 9(a). The predicted BRR/BS, (1.41 $\mu m^3/\mu m^2/day$) was found to be not significantly different from the experimental value of 1.43 ± 0.5675 $\mu m^3/\mu m^2/day$ (p = 0.97, Student's t-test). Endocortical bone loss distribution predicted by the model and the in-vivo experiment have also been shown in Fig 9(c) and 9(b), respectively. It was found that the distribution predicted by the model is not significantly different from the in-vivo distribution (p = 0.99 for Watson's U^2 test).

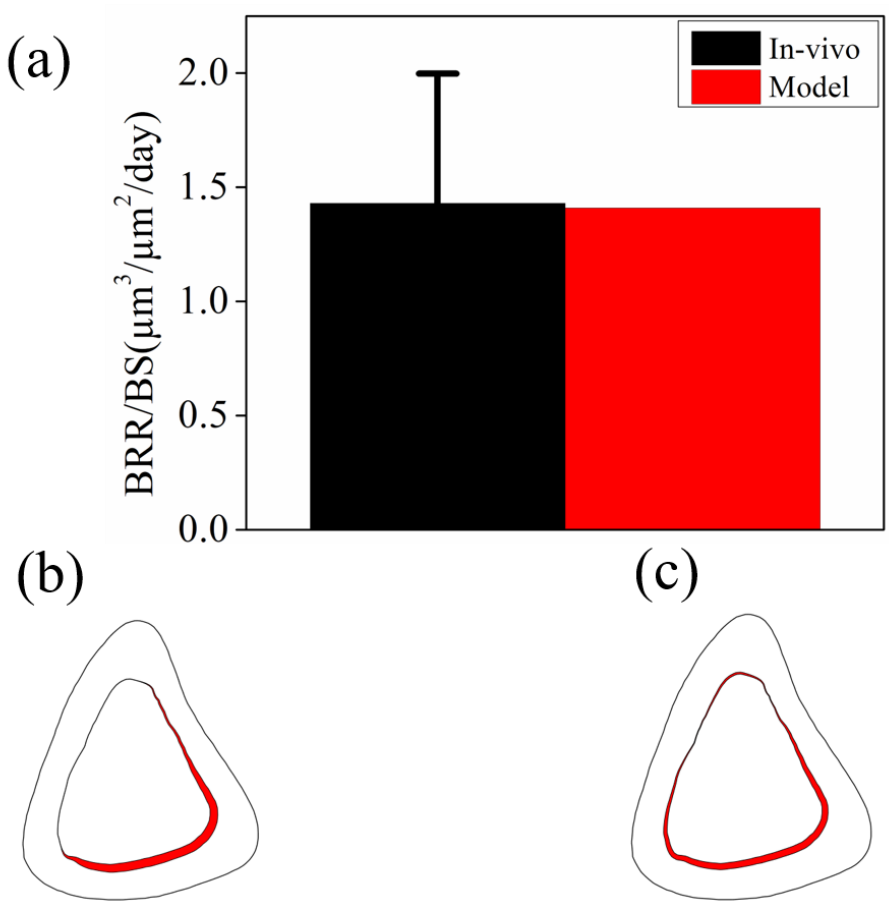

Figure 9: Comparison of the model and the experimental cortical bone loss distribution at the mid-section of a mouse tibia: (a) histogram comparing model BRR/BS to the in-vivo value (error bar represents standard error), (b) in-vivo, site-specific bone loss (shown in red), (c) the bone loss predicted by the model.

3.3 Proximal section

The bone loss at the proximal section of the same tibial bone was predicted using the same resorption coefficient A. The predicted BRR/BS (1.02 $\mu m^3/\mu m^2/\text{day}$) was found to be not significantly different from the corresponding experimental value of 1.23 ± 0.85 (p = 0.80, Student's t-test) as compared in Fig 10(a). The site-specific cortical bone loss distribution predicted by the model (Fig 10(c)) was also found to be significantly different from that of the experimental case (Fig. 10(b)) (p = 0.0004 for Watson's U^2 test). Hence, the model was not able to predict the experimental bone loss distribution for this case.

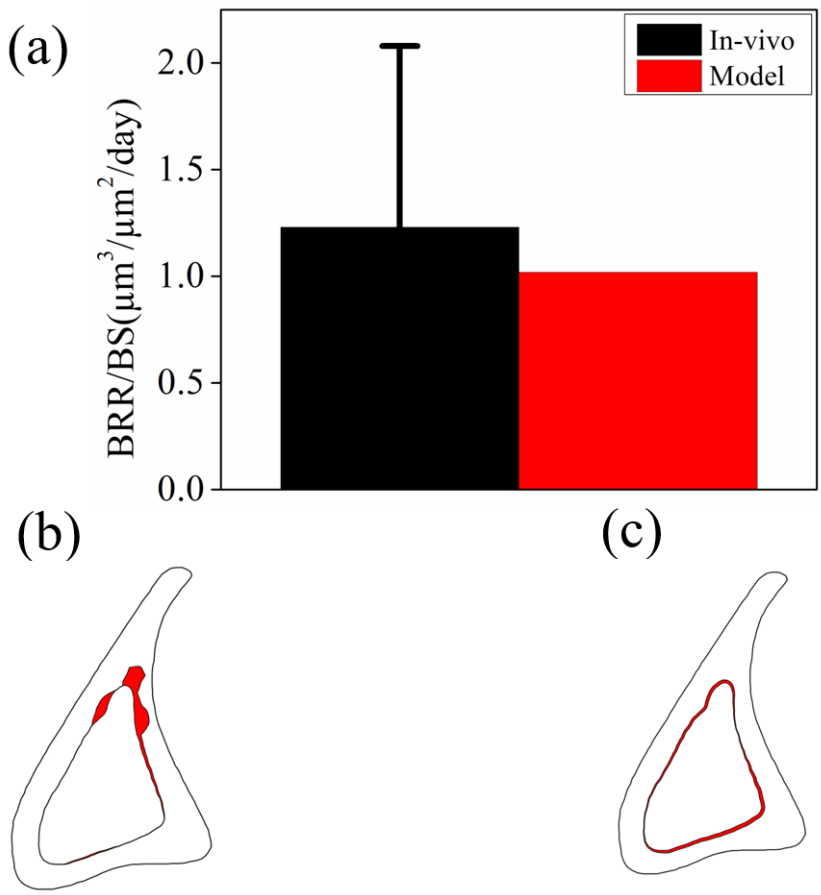

Figure 10: Comparison of model and experimental cortical bone loss at the proximal section of mouse tibia: (a) model BRR/BS has been compared to the in-vivo BRR/BS using a histogram, (b) in-vivo site-specific bone loss (shown in red), (c) bone resorption as predicted by the developed model (shown in red).

3.4 Proximal section incorporating muscle attachments

The results so far were obtained based on the axial loading on tibia, as a simplification of the real scenario where different muscles act at different point of time and for different cage activities. This simplification was able to predict the bone resorption for both distal and mid-diaphyseal sections, as detailed in sections 3.1 and 3.2. Since the model was not able to correctly predict the bone loss at the proximal sections, the effect of muscle activity needs to be incorporated. It is evident from the literature that the four significant muscles viz. flexor digitorum longus (FDL), tibialis posterior (TP), extensor hallucis longus (EHL), and tibialis anterior (TA) are attached (Schaad et al., 2017) close to the considered proximal section, as schematically shown in Fig. 11(a). As no such muscle attachment is seen close to the remaining sections, viz. the distal and mid-section, analysis of the proximal section may need to be done differently and more accurately. This is also in accordance with the Saint Venant Principle (Beer

and Johnston, 1981). Incorporation of muscle activity is complex, however, as there are different cage activities and muscle forces for all these activities are unknown in the existing literature. In view of this, a simple analysis has been carried out just for an example.

These muscles attached close to the proximal section of tibia help in dorsi flexion (TA, EHL) and plantar flexion (TP, FDL) of the ankle during walking and, thus apply load on the bone. The maximum load is carried by the dorsi flexion muscle (Yoon et al., 2013) during a gait cycle. The dorsi flexion muscle includes tibialis anterior (TA) and extensor hallucis longus (EHL). Between these two muscles, TA is prominent due to its higher physiological cross-sectional area (PCSA); hence, only TA was considered during this study. The attachment point of the TA muscle at the proximal section (Fig. 11(b)) is under consideration, and the corresponding muscle force (2.4 N) was obtained from the literature (Charles et al., 2016). The TA muscle force was applied keeping the material property and boundary condition the same as earlier. The corresponding strain pattern and fluid flow pattern obtained by the finite element analysis are shown in Fig. 11(c) and Fig. 11(d) respectively. The experimental and model bone-loss distributions have been shown in Figs. 11(e) and 11(f), respectively. The BRR/BS values have also been compared in Fig. 11(g). The predicted BRR/BS (1.06 $\mu m^3/\mu m^2/$day) was found to be not significantly different from the experimental BRR/BS of 1.23 ± 0.85 (p = 0.84, Student's t-test). The bone loss distribution was also found to be not singnificantly different (p= 0.09, Watson U^2 test). Note that this is only an example showing the importance of incorporation of muscle attachments in the current study. However, due to unavailability of muscle force data for all the cage activity condition, the detailed analysis incorporating the muscle attachments has been taken as a future work.

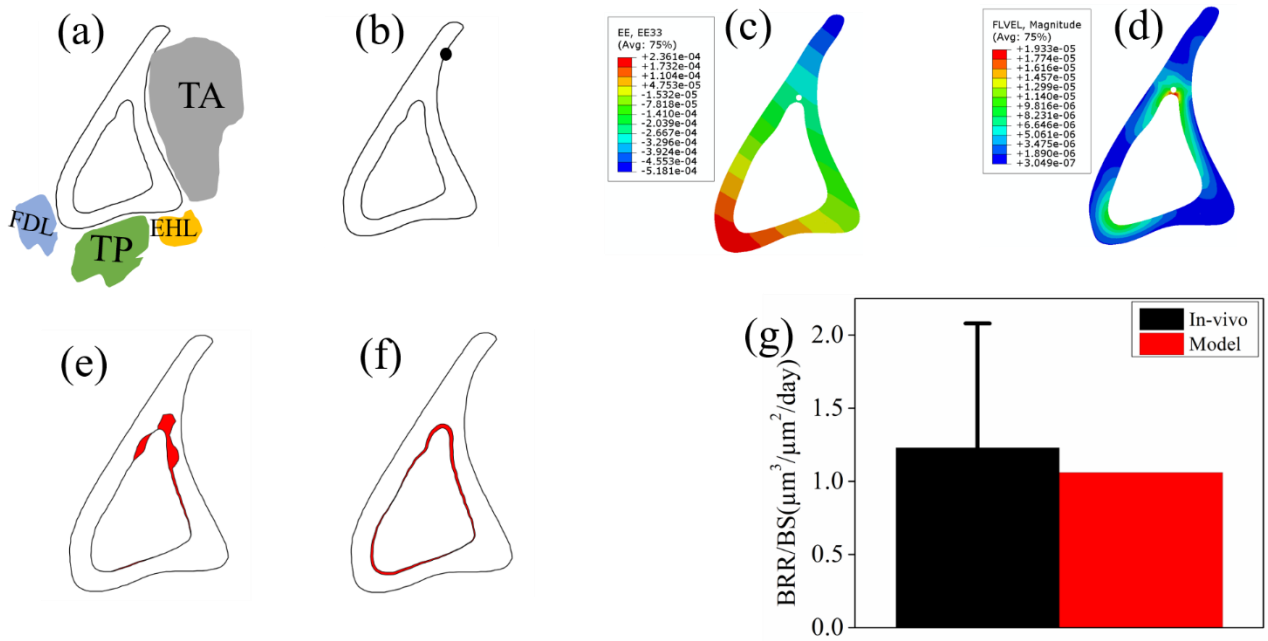

Figure 11: (a) Proximal section with relevant muscles, (b) TA muscle attachment (black dot shows attachment point), (c) axial strain, (d) corresponding fluid velocity (mm/s), (e) in vivo, site-specific bone loss distribution (shown in red), (f) model predicted bone loss (shown in red), (g) histogram compares model BRR/BS to corresponding experimental value.

4. Discussions

The present work studied cortical bone tissue loss due to disuse of the bone. It developed a fluid flow-based mathematical model that utilized the dissipated energy density as a stimulus. A finite element method was used to simulate fluid flow inside the LCN, considering bone as a poroelastic material. The model was fitted to the existing bone loss data in the literature. The developed disuse model showed the linear relation between MRR and the $\sqrt{\phi}$ (i.e., the square root of the dissipation energy density), which is in accordance with the earlier work by Sugiyama et al. (Sugiyama et al., 2012). Note that the dissipation energy density is proportional to the square of strain and, hence, MRR being proportional to $\sqrt{\phi}$ is akin to bone formation rate (BFR) being proportional to the strain (Prasad, 2023). A work by Singh et al. (Singh et al., 2023) has also shown a similar kind of trend, i.e., the rate of new bone formation is directly proportional to the $\sqrt{\phi}$. There would be a new bone formation when the stimulus exceeds the threshold value.

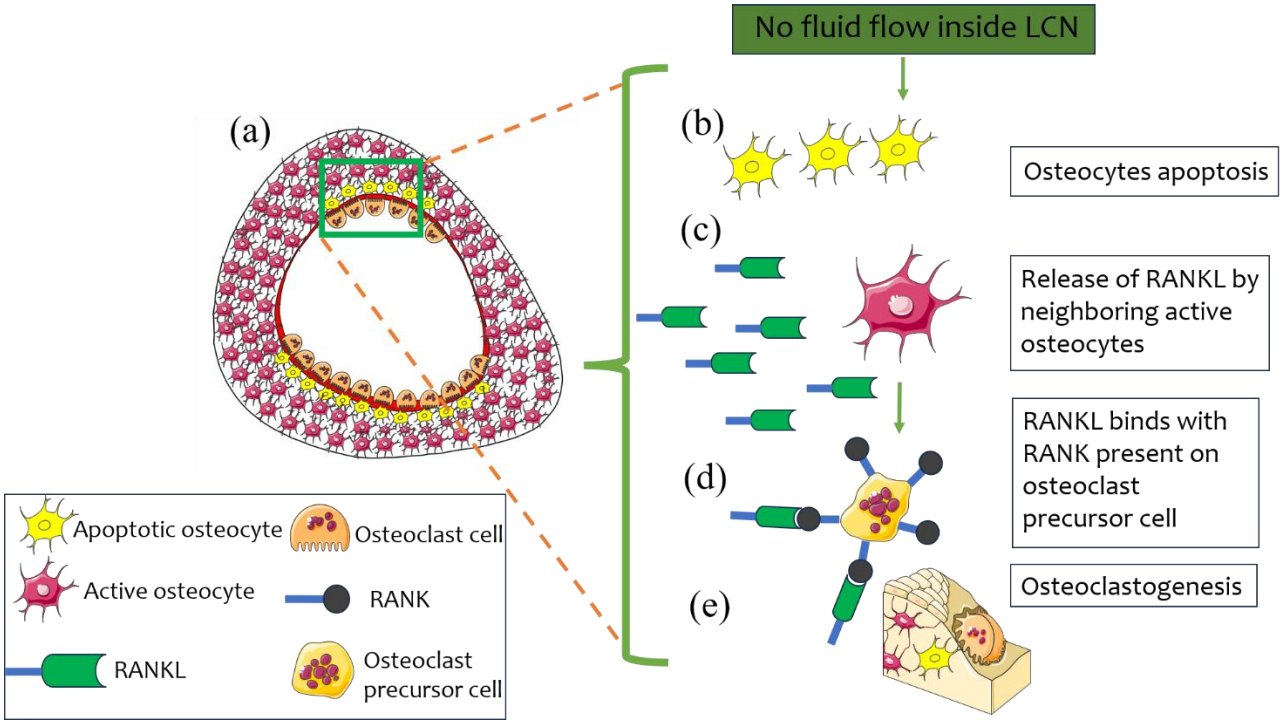

Figure 12: Bone disuse leads to osteoclastogenesis: (a) schematic showing the different bone cell attchement at the section of interest (b) Loss of fluid flow inside the LCN causes osteocyte to apoptosis (c) Active osteocyte near the apoptotic osteocyte release RANKL which, (d) combines with the RANK present on the osteoclast precursor (e) initiation of osteoclasto-genesis by the active osteoclast. (Some parts of this illustration have been created using the Servier medical art, SMART; https://smart.servier.com/)

It has been widely accepted that osteocytes sense the stimulus for the mechano-transduction. The mechanosensory osteocytes need nutrients for survival, which is achieved via load-induced fluid flow inside the LCN. However, in case of bone disuse, there is no fluid flow, which may incapacitate the flow of nutrients inside the LCN. It may also lead to hypoxia inside the LCN. Such an LCN environment is deleterious for osteocyte viability and may cause apoptosis of osteocytes. Dying osteocytes damage the LCN, which becomes the beacon for osteoclast recruitment (Plotkin, 2014) (Xiong et al., 2011). The apoptotic osteocytes further communicate with the neighboring active osteocytes, producing Receptor activator of nuclear factor kappa beta ligand (RANKL), which binds to the Receptor activator of nuclear factor kappa beta (RANK) present on the surface of osteoclast precursor cells. This initiates the osteoclastogenesis as illustrated in Fig. 12. This theory has been supported by in-vivo studies available in the literature. For example, Emerton et al. showed that mouse ovariectomy caused osteocyte apoptosis and, thus, bone loss via formation of active osteoclasts (Emerton et al.,

2010). Another study, in which bone disuse was achieved by tail suspension model presented similar trends where bone tissue loss coincided with the site of apoptotic osteocytes (Aguirre et al., 2006). In a similar study, disuse caused by hindlimb-unloading (via tail suspension) damages the LCN and leads to osteocytic apoptosis resulting into subsequent bone loss (Cabahug-Zuckerman et al., 2016). Although the disuse of bone was achieved via different means, the disuse ultimately caused a loss of stimulus, i.e., a loss of fluid flow inside the LCN. It led to osteocyte -apoptosis and initiated the osteoclastogenesis.

In line with the above studies, the present work has established that the site of maximum bone resorption coincides with that of the maximum stimulus loss, i.e., the maximum loss of dissipation energy density. The developed model predicted cortical bone loss sites at the distal and mid-section of the mouse tibia. However, it could not predict the bone loss distribution at the proximal section. As dicussed in section 3.4, this may be due to a different anatomical arrangement (viz. muscle attachment) of the proximal section as compared to that at the distal and mid-diaphyseal sites (Charles et al., 2016a).

Exogenous loading-induced bone formation in young-adult mice is seen at both the surfaces viz, periosteal and endocortical surface (Srinivasan et al., 2010)(Willie et al., 2013)(Srinivasan et al., 2002)(Birkhold et al., 2016). Accordingly, bone disuse should cause stimulus loss and hence the bone loss at both the surfaces. However, in absence of physiological loading, the bone loss was experimentally found to be at the endocortical surface only (Gross and Rubin, 1995) (Ausk et al., 2012). As two different cells are responsible for bone formation and resorption, i.e., osteoblasts and osteoclasts respectively. It may be possible that, in the case of unloading, these two cells behave differently on the two bone surfaces. Osteoclasts, bone-eating cells, may be more pronounced at the endocortical surface in case of disuse than at the periosteal surface due to the easy access to the bone marrow.

Cortical bone loss due to aging was also limited to the endocortical surface only(Birkhold et al., 2016). Skeletal aging lowered the periosteal deposition; however, no resorption was seen at the outer surface. The earlier study had showed that aging reduced the periosteum thickness significantly (O'Driscoll et al., 2001) (Jimenez-Andrade et al., 2012). The reduced periosteum thickness would, in turn, reduce the pore pressure and thus lower the new bone formation at the periosteal surface, in accordance with the study by Singh et al. Modelling of the age-dependent cortical bone loss has also been takn as a future work.

A study by Gross and Rubin on the turkey's avian wing bone (viz, radius bone) (Gross and Rubin, 1995) reported the bone loss to be uniform along the length and endocortical perimeter. On the other hand, Ausk et al. (Ausk et al., 2012) found that bone loss varies along the length and endocortical perimeter of the mouse tibia. The reason behind this difference may be the difference in structure (curvature, etc.) and loading condition of the two bones (especially torsional loading (Novitskaya et al., 2017), which may be prominent in avian bones, as discussed by Novitskaya et al.). Further work is needed to model the turkey's experimental results. This has also been taken up as a future work.

The developed model predicted the bone loss distribution due to Botox-induced muscle paralysis only. Incorporating the other disuse conditions, such as the tail-suspension model, prolonged bed rest, long space travel, and spinal cord injury, will make the present model robust; however, such experimental data are unavailable in the literature.

Apart from the above, the present model has been developed with several simplifications, as discussed below.

Bone geometry: The present study uses a different prismatic bar for each of the three considered sites (i.e., proximal, mid, and distal). This saves significant computation time; however, analysis of the whole tibia may improve accuracy.

Material properties: The bone is considered a linear isotropic poroelastic material. However, in reality, the bone is highly anisotropic. The cortical bone also has different porosities at different length scales (Cowin, 1999). In the present study, only LCN porosities have been considered. Incorporating all the porosities may enhance the accuracy of the results.

Biological cues: The present model has considered neither bone loss due to natural aging nor the change in the bone's internal architecture due to aging (Sfeir et al., 2022) (Birkhold et al., 2014). Incorporating the aging effect has also been taken into consideration in future work.

5. Conclusions

This work presented a mathematical model for cortical bone loss in disuse conditions. To the author's best knowledge, there has not been such a model in the literature; hence, the developed model is the first of its kind. It takes the loss of stimulus due to the disuse of bone as an input and predicts the cortical bone loss at the site of interest. The theory of poroelasticity was used to compute the fluid flow pattern in the LCN, and the corresponding finite element problem was solved using the ABAQUS software. The developed mathematical model predicted the in-

vivo bone loss for two murine tibial sites (distal and mid-sections), for which data are available in the literature. However, the model could not predict the bone loss distribution at the proximal section, which may be due to muscle attachment close to this section. A detailed analysis for this section, incorporating muscle attachments on the tibia, may be needed and has been taken as a future work. The current model can be improved further by incorporating/predicting other disuse conditions such as extended bed rest, long space travel, and spinal cord injury. However, relevant experimental data will be required for these, which are unavailable in the literature.

References

Abaqus, V., 2014. 6.14. Abaqus Analysis User's Guide. Provid. RI, USA Dassault Syst. Simulia Corp.

Aguirre, J.I., Plotkin, L.I., Stewart, S.A., Weinstein, R.S., Parfitt, A.M., Manolagas, S.C., Bellido, T., 2006. Osteocyte apoptosis is induced by weightlessness in mice and precedes osteoclast recruitment and bone loss. J. Bone Miner. Res. 21, 605–615. https://doi.org/10.1359/jbmr.060107

Ausk, B.J., Huber, P., Poliachik, S.L., Bain, S.D., Srinivasan, S., Gross, T.S., 2012. Cortical bone resorption following muscle paralysis is spatially heterogeneous. Bone 50, 14–22. https://doi.org/10.1016/j.bone.2011.08.028

Beer, F.P. (Ferdinand P., Johnston, E.R. (Elwood R., 1981. Mechanics of materials / Ferdinand P. Beer, E. Russell Johnston, Jr. McGraw-Hill, New York.

Biot, M.A., 1941. General theory of three-dimensional consolidation. J. Appl. Phys. 12, 155–164. https://doi.org/10.1063/1.1712886

Birkhold, A.I., Razi, H., Duda, G.N., Weinkamer, R., Checa, S., Willie, B.M., 2016. The Periosteal Bone Surface is Less Mechano-Responsive than the Endocortical. Sci. Rep. 6, 1–11. https://doi.org/10.1038/srep23480

Birkhold, A.I., Razi, H., Duda, G.N., Weinkamer, R., Checa, S., Willie, B.M., 2014. The influence of age on adaptive bone formation and bone resorption. Biomaterials 35, 9290–9301. https://doi.org/10.1016/j.biomaterials.2014.07.051

Brent, M.B., Brüel, A., Thomsen, J.S., 2021. A Systematic Review of Animal Models of Disuse-Induced Bone Loss. Calcif. Tissue Int. https://doi.org/10.1007/s00223-020-00799-9

Cabahug-Zuckerman, P., Frikha-Benayed, D., Majeska, R.J., Tuthill, A., Yakar, S., Judex, S., Schaffler, M.B., 2016. Osteocyte Apoptosis Caused by Hindlimb Unloading is Required to Trigger Osteocyte RANKL Production and Subsequent Resorption of Cortical and Trabecular Bone in Mice Femurs. J. Bone Miner. Res. 31, 1356–1365. https://doi.org/10.1002/JBMR.2807

Charalambous, C.P., 2014. Humeral hypertrophy in response to exercise. Class. Pap. Orthop. 411–413. https://doi.org/10.1007/978-1-4471-5451-8_104

Charles, J.P., Cappellari, O., Spence, A.J., Hutchinson, J.R., Wells, D.J., 2016a. Musculoskeletal geometry, muscle architecture and functional specialisations of the

mouse hindlimb. PLoS One 11, 1–21. https://doi.org/10.1371/journal.pone.0147669

Charles, J.P., Cappellari, O., Spence, A.J., Wells, D.J., Hutchinson, J.R., 2016b. Muscle moment arms and sensitivity analysis of a mouse hindlimb musculoskeletal model. J. Anat. 229, 514–535. https://doi.org/10.1111/joa.12461

Cowin, S.C., 1999. Bone poroelasticity. J. Biomech. https://doi.org/10.1016/S0021-9290(98)00161-4

Derbyshire, B., 1985. Comment on "Static vs dynamic loads as an influence on bone remodelling." J. Biomech. 18, 729. https://doi.org/10.1016/0021-9290(85)90028-4

Emerton, K.B., Hu, B., Woo, A.A., Sinofsky, A., Hernandez, C., Majeska, R.J., Jepsen, K.J., Schaffler, M.B., 2010. Osteocyte apoptosis and control of bone resorption following ovariectomy in mice. Bone 46, 577–583. https://doi.org/10.1016/j.bone.2009.11.006

Fan, L., Pei, S., Lucas Lu, X., Wang, L., 2016. A multiscale 3D finite element analysis of fluid/solute transport in mechanically loaded bone. Bone Res. 4. https://doi.org/10.1038/boneres.2016.32

Fritton, S.P., Weinbaum, S., 2009. Fluid and Solute Transport in Bone: Flow-Induced Mechanotransduction. Annu. Rev. Fluid Mech. 41, 347–374. https://doi.org/10.1146/ANNUREV.FLUID.010908.165136

Gabel, L., Liphardt, A.M., Hulme, P.A., Heer, M., Zwart, S.R., Sibonga, J.D., Smith, S.M., Boyd, S.K., 2022. Incomplete recovery of bone strength and trabecular microarchitecture at the distal tibia 1 year after return from long duration spaceflight. Sci. Rep. 1–13. https://doi.org/10.1038/s41598-022-13461-1

Gatti, V., Gelbs, M.J., Guerra, R.B., Gerber, M.B., Fritton, S.P., 2021. Interstitial fluid velocity is decreased around cortical bone vascular pores and depends on osteocyte position in a rat model of disuse osteoporosis. Biomech. Model. Mechanobiol. 20, 1135–1146. https://doi.org/10.1007/S10237-021-01438-4/FIGURES/8

Gatti, V., Ghobryal, B., Gelbs, M.J., Gerber, M.B., Doty, S.B., Cardoso, L., Fritton, S.P., 2019. Botox-induced muscle paralysis alters intracortical porosity and osteocyte lacunar density in skeletally mature rats. J. Orthop. Res. 37, 1153–1163. https://doi.org/10.1002/JOR.24276

Gross, T.S., Rubin, C.T., 1995. Uniformity of resorptive bone loss induced by disuse. J. Orthop. Res. 13, 708–714. https://doi.org/10.1002/jor.1100130510

Gururaja, S., Kim, H.J., Swan, C.C., Brand, R.A., Lakes, R.S., 2005. Modeling deformation-induced fluid flow in cortical bone's canalicular-lacunar system. Ann. Biomed. Eng. 33, 7–25. https://doi.org/10.1007/s10439-005-8959-6

Haapasalo, H., Kontulainen, S., Sievänen, H., Kannus, P., Järvinen, M., Vuori, I., 2000. Exercise-induced bone gain is due to enlargement in bone size without a change in volumetric bone density: A peripheral quantitative computed tomography study of the upper arms of male tennis players. Bone 27, 351–357. https://doi.org/10.1016/S8756-3282(00)00331-8

Hargens, A.R., Vico, L., 2016. Long-duration bed rest as an analog to microgravity. J. Appl. Physiol. https://doi.org/10.1152/japplphysiol.00935.2015

Hasriadi, Wasana, P.W.D., Vajragupta, O., Rojsitthisak, P., Towiwat, P., 2021. Automated

home-cage monitoring as a potential measure of sickness behaviors and pain-like behaviors in LPS-treated mice. PLoS One 16, e0256706. https://doi.org/10.1371/JOURNAL.PONE.0256706

Huddleston, A.L., Rockwell, D., Kulund, D.N., 1980. Bone Mass in Lifetime Tennis Athletes. JAMA J. Am. Med. Assoc. 244, 1107–1109. https://doi.org/10.1001/jama.1980.03310100025022

Jimenez-Andrade, J.M., Mantyh, W.G., Bloom, A.P., Freeman, K.T., Ghilardi, J.R., Kuskowski, M.A., Mantyh, P.W., 2012. The effect of aging on the density of the sensory nerve fiber innervation of bone and acute skeletal pain. Neurobiol. Aging 33, 921–932. https://doi.org/10.1016/j.neurobiolaging.2010.08.008

Klein-Nulend, J., Bakker, A.D., Bacabac, R.G., Vatsa, A., Weinbaum, S., 2013. Mechanosensation and transduction in osteocytes. Bone 54, 182–190. https://doi.org/10.1016/j.bone.2012.10.013

Kumar, N.C., Jasiuk, I., Dantzig, J., 2011. Dissipation energy as a stimulus for cortical bone adaptation. J. Mech. Mater. Struct. 6, 303–319. https://doi.org/10.2140/jomms.2011.6.303

Lang, T., LeBlanc, A., Evans, H., Lu, Y., Genant, H., Yu, A., 2004. Cortical and trabecular bone mineral loss from the spine and hip in long-duration spaceflight. J. Bone Miner. Res. 19, 1006–1012. https://doi.org/10.1359/JBMR.040307

Lee, T.Q., Shapiro, T.A., Bell, D.M., 1997. Biomechanical properties of human tibias in long-term spinal cord injury. J. Rehabil. Res. Dev. 34, 295–302.

Levenberg, K., 1944. A method for the solution of certain non-linear problems in least squares. Q. Appl. Math. 2, 164–168. https://doi.org/10.1090/qam/10666

Mertiya, A.S., Tiwari, A.K., Mishra, A., Main, R.P., Tripathi, D., Tiwari, A., 2022. Computational modeling for osteogenic potential assessment of physical exercises based on loading-induced mechanobiological environments in cortical bone remodeling. Biomech. Model. Mechanobiol. https://doi.org/10.1007/s10237-022-01647-5

Meslier, Q.A., Shefelbine, S.J., 2023. Using Finite Element Modeling in Bone Mechanoadaptation 105–116. https://doi.org/10.1007/s11914-023-00776-9

Novitskaya, E., Ruestes, C.J., Porter, M.M., Lubarda, V.A., Meyers, M.A., McKittrick, J., 2017. Reinforcements in avian wing bones: Experiments, analysis, and modeling. J. Mech. Behav. Biomed. Mater. 76, 85–96. https://doi.org/10.1016/j.jmbbm.2017.07.020

O'Driscoll, S.W.M., Saris, D.B.F., Ito, Y., Fitzimmons, J.S., 2001. The chondrogenic potential of periosteum decreases with age. J. Orthop. Res. 19, 95–103. https://doi.org/10.1016/S0736-0266(00)00014-0

Patel, T.K., Brodt, M.D., Silva, M.J., 2014. Experimental and finite element analysis of strains induced by axial tibial compression in young-adult and old female C57Bl/6 mice. J. Biomech. 47, 451–457. https://doi.org/10.1016/j.jbiomech.2013.10.052

Pereira, A.F., Javaheri, B., Pitsillides, A.A., Shefelbine, S.J., 2015. Predicting cortical bone adaptation to axial loading in the mouse tibia. J. R. Soc. Interface 12. https://doi.org/10.1098/rsif.2015.0590

Plotkin, L.I., 2014. Apoptotic osteocytes and the control of targeted bone resorption. Curr.

Osteoporos. Rep. 12, 121–126. https://doi.org/10.1007/s11914-014-0194-3

Prasad, J., 2023. Relating strain amplitude, strain threshold and bone formation rate to exogenous forcing frequency. bioRxiv 2023.10.08.561406. https://doi.org/10.1101/2023.10.08.561406

Prasad, J., Wiater, B.P., Nork, S.E., Bain, S.D., Gross, T.S., 2010. Characterizing gait induced normal strains in a murine tibia cortical bone defect model. J. Biomech. 43, 2765–2770. https://doi.org/10.1016/j.jbiomech.2010.06.030

Qin, L., Liu, W., Cao, H., Xiao, G., 2020. Molecular mechanosensors in osteocytes. Bone Res. 8, 1–24. https://doi.org/10.1038/s41413-020-0099-y

Rittweger, J., Frost, H.M., Schiessl, H., Ohshima, H., Alkner, B., Tesch, P., Felsenberg, D., 2005. Muscle atrophy and bone loss after 90 days' bed rest and the effects of flywheel resistive exercise and pamidronate: Results from the LTBR study. Bone 36, 1019–1029. https://doi.org/10.1016/J.BONE.2004.11.014

Rittweger, J., Simunic, B., Bilancio, G., Gaspare De Santo, N., Cirillo, M., Biolo, G., Pisot, R., Eiken, O., Mekjavic, I.B., Narici, M., 2009. Bone loss in the lower leg during 35 days of bed rest is predominantly from the cortical compartment. Bone 44, 612–618. https://doi.org/10.1016/J.BONE.2009.01.001

Rolvien, T., Amling, M., 2021. Disuse Osteoporosis: Clinical and Mechanistic Insights. Calcif. Tissue Int. https://doi.org/10.1007/s00223-021-00836-1

Schaad, L., Hlushchuk, R., Barré, S., Gianni-Barrera, R., Haberthür, D., Banfi, A., Djonov, V., 2017. Correlative Imaging of the Murine Hind Limb Vasculature and Muscle Tissue by MicroCT and Light Microscopy. Sci. Rep. 7, 1–12. https://doi.org/10.1038/srep41842

Sfeir, J.G., Drake, M.T., Khosla, S., Farr, J.N., 2022. Skeletal Aging. Mayo Clin. Proc. 97, 1194–1208. https://doi.org/10.1016/J.MAYOCP.2022.03.011

Singh, S., Singh, S.J., Prasad, J., 2023. Derivation, Validation, and Prediction of Loading-Induced Mineral Apposition Rates at Endocortical and Periosteal Bone Surfaces Based on Fluid Velocity and Pore Pressure. bioRxiv 2023.09.08.556956. https://doi.org/10.1101/2023.09.08.556956

Smit, T.H., 2022. Finite Element Models of Osteocytes and Their Load-Induced Activation. Curr. Osteoporos. Reports 2022 202 20, 127–140. https://doi.org/10.1007/S11914-022-00728-9

Srinivasan, S., Ausk, B.J., Prasad, J., Threet, D., Bain, S.D., Richardson, T.S., Gross, T.S., 2010. Rescuing loading induced bone formation at senescence. PLoS Comput. Biol. 6. https://doi.org/10.1371/journal.pcbi.1000924

Srinivasan, S., Weimer, D.A., Agans, S.C., Bain, S.D., Gross, T.S., 2002. Low-magnitude mechanical loading becomes osteogenic when rest is inserted between each load cycle. J. Bone Miner. Res. 17, 1613–1620. https://doi.org/10.1359/jbmr.2002.17.9.1613

Steck, R., Niederer, P., Knothe Tate, M.L., 2003. A finite element analysis for the prediction of load-induced fluid flow and mechanochemical transduction in bone. J. Theor. Biol. 220, 249–259. https://doi.org/10.1006/JTBI.2003.3163

Sugiyama, T., Meakin, L.B., Browne, W.J., Galea, G.L., Price, J.S., Lanyon, L.E., 2012.

Bones' adaptive response to mechanical loading is essentially linear between the low strains associated with disuse and the high strains associated with the lamellar/woven bone transition. J. Bone Miner. Res. 27, 1784–1793. https://doi.org/10.1002/JBMR.1599

Teresa, M., Anchez, S.´, Angeles, M., Erez, P.´, José, ·, José, J., García-Aznar, M., 2020. The role of fluid flow on bone mechanobiology: mathematical modeling and simulation. Comput. Geosci. 2020 252 25, 823–830. https://doi.org/10.1007/S10596-020-09945-6

Tiwari, A.K., Prasad, J., 2017. Computer modelling of bone's adaptation: the role of normal strain, shear strain and fluid flow. Biomech. Model. Mechanobiol. 16, 395–410. https://doi.org/10.1007/s10237-016-0824-z

Van Tol, A.F., Schemenz, V., Wagermaier, W., Roschger, A., Razi, H., Vitienes, I., Fratzl, P., Willie, B.M., Weinkamer, R., 2020. The mechanoresponse of bone is closely related to the osteocyte lacunocanalicular network architecture. Proc. Natl. Acad. Sci. U. S. A. 117, 32251–32259. https://doi.org/10.1073/pnas.2011504117

Verbruggen, S.W., Vaughan, T.J., McNamara, L.M., 2014. Fluid flow in the osteocyte mechanical environment: a fluid-structure interaction approach. Biomech. Model. Mechanobiol. 13, 85–97. https://doi.org/10.1007/S10237-013-0487-Y

Vico, L., Collet, P., Guignandon, A., Lafage-Proust, M.H., Thomas, T., Rehailia, M., Alexandre, C., 2000. Effects of long-term microgravity exposure on cancellous and cortical weight-bearing bones of cosmonauts. Lancet (London, England) 355, 1607–1611. https://doi.org/10.1016/S0140-6736(00)02217-0

Warden, S.J., Mantila Roosa, S.M., Kersh, M.E., Hurd, A.L., Fleisig, G.S., Pandy, M.G., Fuchs, R.K., 2014. Physical activity when young provides lifelong benefits to cortical bone size and strength in men. Proc. Natl. Acad. Sci. U. S. A. 111, 5337–5342. https://doi.org/10.1073/pnas.1321605111

WATSON, G.S., 1961. Goodness-of-fit tests on a circle. Biometrika 48, 109–114. https://doi.org/10.1093/biomet/48.1-2.109

Weinbaum, S., Cowin, S.C., Zeng, Y., 1994. A model for the excitation of osteocytes by mechanical loading-induced bone fluid shear stresses. J. Biomech. 27, 339–360. https://doi.org/10.1016/0021-9290(94)90010-8

Willie, B.M., Birkhold, A.I., Razi, H., Thiele, T., Aido, M., Kruck, B., Schill, A., Checa, S., Main, R.P., Duda, G.N., 2013. Diminished response to in vivo mechanical loading in trabecular and not cortical bone in adulthood of female C57Bl/6 mice coincides with a reduction in deformation to load. Bone 55, 335–346. https://doi.org/10.1016/j.bone.2013.04.023

Xiong, J., Onal, M., Jilka, R.L., Weinstein, R.S., Manolagas, S.C., O'Brien, C.A., 2011. Matrix-embedded cells control osteoclast formation. Nat. Med. 17, 1235–1241. https://doi.org/10.1038/nm.2448

Yoon, J.Y., An, D.Hy., Oh, J.S., 2013. Plantarflexor and dorsiflexor activation during inclined walking with and without modified mobilization with movement using tape in women with limited ankle dorsiflexion. J. Phys. Ther. Sci. 25, 993–995. https://doi.org/10.1589/jpts.25.993

Zhou, X., Novotny, J.E., Wang, L., 2008. Modeling fluorescence recovery after photobleaching in loaded bone: Potential applications in measuring fluid and solute

transport in the osteocytic lacunar-canalicular system. Ann. Biomed. Eng. 36, 1961–1977. https://doi.org/10.1007/s10439-008-9566-0